

Anti-aligning interaction between active particles induces a finite wavelength instability: The dancing hexagons

Daniel Escaff *Universidad de los Andes, Chile, Avenida Monseñor Álvaro del Portillo N° 12.455, Las Condes, Santiago 7620060, Chile*

(Received 29 July 2023; revised 15 October 2023; accepted 11 January 2024; published 6 February 2024)

By considering a simple model for self-propelled particle interaction, we show that anti-aligning forces induce a finite wavelength instability. Consequently, the system exhibits pattern formation. The formed pattern involves, let us say, a choreographic movement of the active entities. At the level of particle density, the system oscillates between a stripe pattern and a hexagonal one. The underlying dynamics of these density oscillations consists of two counterpropagating and purely hexagonal traveling waves. They are assembling and disassembling a global hexagonal structure and a striped lineup of particles. This self-assembling process becomes quite erratic for long-time simulations, seeming aperiodic.

DOI: [10.1103/PhysRevE.109.024602](https://doi.org/10.1103/PhysRevE.109.024602)

I. INTRODUCTION

The capability of out-of-equilibrium entities to exhibit collective behaviors has captured the attention of scientists for decades. For example, the appropriate coupling of out-of-equilibrium oscillators may lead to synchronization, where the collective oscillates as a single oscillator. In 1975, Kuramoto [1,2] proposed a phase equation that traps the main features of synchronization near the critical point where the system starts to self-organize. This model has become one of the main paradigms of out-of-equilibrium self-organization [3–6].

Another paradigmatic example is the chemical origin of morphogenesis. Reacting chemical species may undergo a finite wavelength instability of their densities, forming spatially structured patterns. Earlier reported by Zeldovich [7], this mechanism became popular after the works of Turing [8] and, later, the Brussels school [9]. Afterward, the idea of finite wavelength instabilities (first used in the context of hydrodynamics [10]) has been applied to many different systems, such as nonlinear optic [11] or population dynamics [12,13], just to mention some examples (see Ref. [14] for a comprehensive review).

In the context of active matter, the starting paradigm is Vicsek's model [15]. It is a simple model that captures the essential features of the flocking transition, that is, how a set of self-propelled entities can synchronize to move in unison. It is simple for numerical studies but complicated for analytical investigations. Consequently, during the 2000s, there was much debate about the nature of the flocking transition: Is it a first- or second-order transition [16]? In fact, Vicsek's model has strong size effects; it is pretty sensitive to discretization (it is a discrete-time stochastic dynamics) and how noise is introduced. More recently, a kinetic theory for Vicsek-type microscopic rules has been developed [17,18].

Here, we will consider a Kuramoto-type of interaction, sometimes called a continuous-time variant of Vicsek's model [19], which is more suitable for analytical explorations. For aligning interaction, this model exhibits a zero wave number

(or infinite wavelength) instability that leads to flocking transition [19,20]. It is a second-order transition for large interaction ranges, leading to a spatially uniform flux. While for short interaction ranges, the transition becomes first order, leading to clusterization [20]. The last process might be related to a spinodal decomposition similar to the one reported for Vicsek's model [21]. Furthermore, this model can exhibit pattern formation if a density-dependent speed is considered [19]; the formation mechanism is highly nonlinear and is not associated with linear instabilities. These patterns might be related to the ones observed in a lattice variant of Vicsek's model [22]. On the other hand, finite wavelength instabilities can be observed in conservative generalizations of this interaction [20] (which induce cohesive forces). The transition is highly subcritical, leading to a spinodal decomposition that ends in a single self-propelled cluster. Moreover, apolar generalizations of this type of interaction lead to the formation of counterpropagating clusters, which collide, behaving as dissipative solitons [23]. In addition, including a phase shift in the Kuramoto-like interaction term, the system may form self-propelled chimeras [24]. Furthermore, by considering chiral Kuramoto-type active particles with randomly distributed frequencies, synchronized rotations have been observed, and opposite chirality cooperation of particles [25]. It is worth mentioning that, using a similar velocity-aligning force, it has been reported that simple Brownian particles (non-self-propelled particles, which are just driven by fluctuations) can also exhibit collective motion [26].

In this paper, we will address the case of anti-aligning interaction (some kind of antiferromagnetic interaction, if the magnetic analogy applies). Although one may speculate that no macroscopic self-organization is expected, there is evidence that antisynchronous interactions might lead to the formation of oscillatory patterns in out-of-equilibrium systems. For instance, a mixed population of globally coupled Kuramoto oscillators, ones with synchronous coupling (conformists) and the others with antisynchronous one (contrarians), might exhibit surprising self-organized behaviors,

as the formation of an oscillatory phase [27]. In the context of Vicsek's model, including anti-alignment as fluctuations may induce a zero wave-number Hopf bifurcation, leading to oscillating time-dependent flockings [28]. Another example is the case of lattices of Wood-type [29] three-state stochastic oscillators. Although waving patterns can be observed in such lattices for synchronous interactions [30], antisynchronous coupling induces a finite wavelength instability, which leads to the formation of traveling waves [31].

The paper is organized as follows. In Sec. II, we show that the Kuramoto-type model has a finite wavelength instability for negative coupling (anti-aligning interaction). The instability takes place with a nonzero imaginary part of the critical modes (it is a type- I_0 instability in the Cross-Hohenberg nomenclature [14]). In Sec. III, we present some numerical observations above the instability. The formed pattern consists of two counterpropagating hexagonal traveling waves, which are assembling and disassembling a global hexagonal structure and a striped lineup of particles. Because of this choreographic movement of the active particles, we call this dissipative structure the dancing hexagons. In Sec. IV, we analyze the spatiotemporal dynamics of the dancing hexagons, showing that the self-assembling process is quite erratic in time, seeming aperiodic. In Sec. V, we perform a brief numerical exploration in Vicsek's model, finding dancing hexagons for anti-aligning interaction. In Sec. VI, we present our conclusions, remarks, and future perspectives.

II. FINITE WAVELENGTH INSTABILITY FOR ANTI-ALIGNING INTERACTION

Let us consider a set of N self-propelled particles, characterized by their positions $\{\vec{r}_l\}_{l=1}^N$ (in two dimensions), and the orientation angles $\{\theta_l\}_{l=1}^N$. Each particle moves with a constant speed v in the direction $\hat{\theta}_l = (\cos \theta_l, \sin \theta_l)$, and obeys the equations of motion

$$\dot{\vec{r}}_l = v\hat{\theta}_l, \quad (1)$$

$$\dot{\theta}_l = \frac{a}{\pi\sigma^2} \sum_{\vec{r}_j \in \mathcal{D}_\sigma(\vec{r}_l)} \sin(\theta_j - \theta_l) + \sqrt{\eta}\xi_l(t), \quad (2)$$

where $\mathcal{D}_\sigma(\vec{r})$ represents a circular domain of radius σ and centered in the position \vec{r} . $\xi_l(t)$ are independent Gaussian white noises, $\langle \xi_l(t) \rangle = 0$ and $\langle \xi_j(t')\xi_l(t) \rangle = \delta_{jl}\delta(t' - t)$. η is the noise intensity. The parameter a is related to the coupling strength, normalized by the area of the circle.

Aligning forces are characterized by $a > 0$. That is, for the pair $\{l, j\}$ interaction, the configuration $\theta_j - \theta_l = 0$ is an attractor, while $\theta_j - \theta_l = \pm\pi$ is repulsive. For that reason, this type of interaction promotes a global flocking [19,20]. On the other hand, anti-alignment tendencies are related to $a < 0$ (attractive $\theta_j - \theta_l = \pm\pi$ and repulsive $\theta_j - \theta_l = 0$). In this paper, we will focus on the last case.

At the macroscopic level, the system may be described by the particle density

$$n(\vec{r}, \theta, t) = \sum_{l=1}^N \delta(\vec{r}_l(t) - \vec{r})\delta(\theta_l(t) - \theta). \quad (3)$$

Neglecting the inherent fluctuations of a finite N ensemble (which typically scales as \sqrt{N}), the interaction term may be approached by its mean value

$$\begin{aligned} & \sum_{\vec{r}_j \in \mathcal{D}_\sigma(\vec{r}_i)} \sin(\theta_j - \theta_i) \\ &= \int_{\mathcal{D}_\sigma(\vec{r})} d^2r' \int_0^{2\pi} d\theta' n(\theta', \vec{r}', t) \sin(\theta' - \theta) \\ &\approx N \int_{\mathcal{D}_\sigma(\vec{r})} d^2r' \int_0^{2\pi} d\theta' \rho(\theta', \vec{r}', t) \sin(\theta' - \theta), \end{aligned}$$

where ρ corresponds to the one-particle probability distribution. At this level of approximation ρ satisfies the nonlinear Fokker-Planck equation

$$\frac{\partial \rho}{\partial t} = -v\hat{\theta} \cdot \vec{\nabla}_{\vec{r}} \rho + \frac{\eta}{2} \frac{\partial^2 \rho}{\partial \theta^2} - \frac{\partial}{\partial \theta} \{\rho \mathcal{T} \rho\}, \quad (4)$$

where $\hat{\theta} = (\cos \theta, \sin \theta)$ and

$$\mathcal{T} \rho = aN \int_{\mathcal{D}_\sigma(\vec{r})} \frac{d^2r'}{\pi\sigma^2} \int_0^{2\pi} d\theta' \rho(\theta', \vec{r}', t) \sin(\theta' - \theta).$$

The asynchronous state is represented by the uniform distribution

$$\rho = \frac{1}{2\pi A},$$

where A is the area occupied by the system. Introducing a perturbation in the Fourier space

$$\rho(\theta, \vec{r}, t) = \frac{1}{2\pi A} + \bar{\epsilon} \exp(\lambda(k)t + i\vec{k} \cdot \vec{r})\Phi(\theta),$$

with $k = |\vec{k}|$, and linearizing respect to the small perturbation parameter $\bar{\epsilon}$, it is obtained a eigenvalues problem to compute the $\lambda(k)$ spectrum [20],

$$(\mathcal{L}_0 - ivk\mathcal{L}_1)\Phi = \lambda(k)\Phi, \quad (5)$$

\mathcal{L}_0 is diagonal in the basis $\{e^{im\theta}\}_{m=-\infty}^{\infty}$,

$$\mathcal{L}_0 e^{im\theta} = \lambda_m^{[0]}(k) e^{im\theta},$$

with the eigenvalues

$$\lambda_m^{[0]}(k) = -\frac{\eta}{2}m^2 + n_0 a \left(\frac{J_1(k\sigma)}{k\sigma} \right) (\delta_{m,1} + \delta_{m,-1}), \quad (6)$$

where $n_0 = N/A$ is the global density, and J_1 is a Bessel function of the first kind. On the other hand,

$$\mathcal{L}_1 e^{im\theta} = (e^{i(m+1)\theta} + e^{i(m-1)\theta})/2,$$

where, without loss of generality, we have defined the orientation angle θ respect to de direction \vec{k} .

Therefore, the asynchronous state is stable if $\text{Re}[\lambda(k)] \leq 0$ for any value of the wave number k . For $k = 0$, the $\lambda(k)$ spectrum corresponds to Eq. (6), and $\lambda_0^{[0]}(0) = 0$ always, which is related to the conservation of the number of particles. For aligning interaction $a > 0$, the modes $m = \pm 1$ destabilize for $k = 0$ and $n_0 a_c = \eta$, leading to flocking transition [20].

A finite wavelength instability occurs when $\text{Re}[\lambda(k)]$ becomes positive for a values $k \neq 0$, and remains negative for the rest. It does not happen for aligning interaction $a > 0$ [19,20]. Although conservative generalizations of this interaction might induce this type of instabilities for $a > 0$ [20],

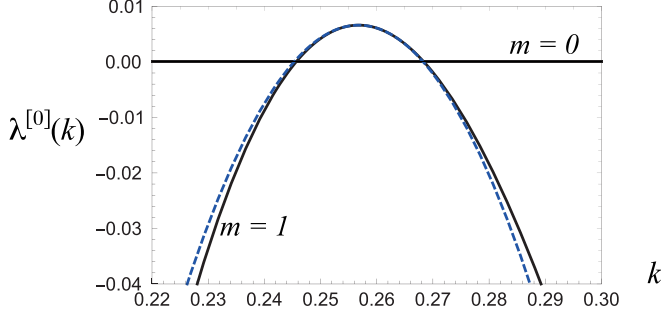


FIG. 1. $\lambda_m^{[0]}(k)$ from Eq. (6), for $m = \pm 1$ and $m = 0$. $\sigma = 20$, $\eta = 0.5$, and $n_0 a = n_0 a_c - 0.1$, with $n_0 a_c \cong -3.78$. The dashed curve corresponds to the parabolic approximation $\varepsilon(k)$ defined by Eq. (9).

they involve cohesive forces that bring about a highly subcritical transition, which leads to a spinodal decomposition that always ends in a single self-propelled cluster.

Here, we will explore the possibility of finite wavelength instabilities for the case of anti-aligning interaction $a < 0$. Taking a as the control parameter, the critical condition is

$$a = a_c \Rightarrow \text{Re}[\lambda(k_c)] = 0 \text{ and } \text{Re}[\lambda(k)] < 0 \forall k \neq k_c,$$

which implies that $\text{Re}[\lambda(k_c)]$ is a maximum,

$$\left. \frac{\partial \text{Re}[\lambda(k)]}{\partial k} \right|_{k=k_c} = 0 \text{ and } \left. \frac{\partial^2 \text{Re}[\lambda(k)]}{\partial k^2} \right|_{k=k_c} < 0.$$

A. Without self-propulsion

For $v = 0$, the $\lambda(k)$ spectrum corresponds to Eq. (6). Here, the modes with $m \neq \pm 1$ do not depend on the wave number k . Therefore, only the modes with $m = \pm 1$ can destabilize. For anti-aligning interaction $a < 0$, $\lambda_1^{[0]}(0) < 0$ always. However, as shown in Fig. 1, the system may undergo a finite wavelength instability.

At the critical point

$$\lambda_1^{[0]}(k_c) = 0 \text{ and } \left. \frac{\partial \lambda_1^{[0]}(k)}{\partial k} \right|_{k=k_c} = 0,$$

which are equations to determine k_c and a_c . The critical wave number, then, satisfies the equation

$$J_2(k_c \sigma) + \frac{2J_1(k_c \sigma)}{k_c \sigma} - J_0(k_c \sigma) = 0,$$

which must be solved numerically, obtaining

$$k_c = \frac{\gamma}{\sigma} \text{ with } \gamma \cong 5.13562. \quad (7)$$

Hence, the critical condition takes the form

$$\frac{n_0 a_c}{\eta} = \frac{k_c \sigma}{2J_1(k_c \sigma)} \cong -7.59975. \quad (8)$$

Near the instability and close to the critical wave number, we may approach the spectrum by the parabola

$$\lambda_1^{[0]}(k) \approx \varepsilon(k) = -C n_0 (a - a_c) - \frac{\eta}{4} [(k - k_c) \sigma]^2, \quad (9)$$

where $C = -J_1(k_c \sigma)/(k_c \sigma) \cong 0.066$. Figure 1 shows how this parabolic approximation (dashed curve) fits with $\lambda_1^{[0]}(k)$.

B. With self-propulsion

1. Diffusive effect of the speed for arbitrarily large wavelength perturbations

Now, all the modes may depend on the wave number k . $\lambda_0^{[0]}(k)$ is zero only for $k = 0$. If its real part becomes positive for arbitrary small k (or arbitrary large wavelength), the system typically develops a coarsening dynamics, where the active particles tend to form a single cluster [32]. It is counterintuitive that anti-aligning interaction, without cohesive forces, will lead to this type of behavior. To discard it, let us consider the effect of a small k in the mode $m = 0$ perturbatively.

To do this, we introduce the inner product

$$\langle \phi | \psi \rangle = \frac{1}{2\pi} \int_0^{2\pi} \phi(\theta)^* \psi(\theta) d\theta,$$

and the Dirac notation

$$e^{im\theta} = |m\rangle \Rightarrow \langle m | m' \rangle = \delta_{m,m'}.$$

Then, the linear problem (5), for the mode $m = 0$, can be written as

$$(\mathcal{L}_0 - ivk\mathcal{L}_1) \sum_{n=0}^{\infty} |\phi^{[n]}\rangle = (\lambda_0^{[1]} + \lambda_0^{[2]} + \dots) \sum_{n=0}^{\infty} |\phi^{[n]}\rangle,$$

where,

$$\mathcal{L}_0 = \sum_{m=-\infty}^{\infty} \lambda_m^{[0]}(k) |m\rangle \langle m|,$$

$$\mathcal{L}_1 = \frac{1}{2} \sum_{m=-\infty}^{\infty} (|m+1\rangle \langle m| + |m-1\rangle \langle m|),$$

and $|\phi^{[n]}\rangle \sim \lambda_0^{[n]} \sim k^n$.

Then, the order zero gives

$$\mathcal{L}_0 |\phi^{[0]}\rangle = 0 \Rightarrow |\phi^{[0]}\rangle = |0\rangle.$$

The first order gives

$$\mathcal{L}_0 |\phi^{[1]}\rangle = [\lambda_0^{[1]} + ivk\mathcal{L}_1] |\phi^{[0]}\rangle.$$

Hence,

$$\lambda_0^{[1]} = -ivk \langle 0 | \mathcal{L}_1 | 0 \rangle = 0 \Rightarrow |\phi^{[1]}\rangle = \frac{ivk}{2\lambda_1^{[0]}(0)} (|1\rangle + |-1\rangle).$$

The second order gives

$$\mathcal{L}_0 |\phi^{[2]}\rangle = \lambda_0^{[2]} |\phi^{[0]}\rangle + ivk\mathcal{L}_1 |\phi^{[1]}\rangle.$$

And then,

$$\lambda_0^{[2]} = -ivk \langle 0 | \mathcal{L}_1 |\phi^{[1]}\rangle = -\left(\frac{v^2}{\eta - n_0 a}\right) k^2. \quad (10)$$

Therefore, near $k = 0$, and for anti-aligning interaction $a < 0$, the $m = 0$ mode exhibits the diffusion spectrum $\lambda \approx -Dk^2$, with $D > 0$. That is, large-wavelength perturbations are stabilized.

2. Finite wavelength instability for low speed

Now, we will analyze the effect of the speed v in the finite wave instability. More precisely, we will perturb the critical point obtained in the previous section, taking $v \sim \varepsilon(k)$. In this case, the linear problem (5) can be written as

$$[\mathcal{L}_0^c + (\varepsilon(k)\Delta\mathcal{L}_0 - ivk_c\mathcal{L}_1)]|\Phi\rangle = \lambda(k)|\Phi\rangle,$$

where

$$\mathcal{L}_0^c = -\frac{\eta}{2} \sum_{m=2}^{\infty} m^2 (|m\rangle\langle m| + |-m\rangle\langle -m|)$$

is the linear operator at the critical point for zero speed. That is, at

$$a = a_c \Rightarrow \lambda_{\pm 1}^{[0]}(k_c) = \lambda_0^{[0]}(k_c) = 0.$$

And

$$\Delta\mathcal{L}_0 = |1\rangle\langle 1| + |-1\rangle\langle -1|.$$

Then, we expand

$$|\Phi\rangle = |\phi^{(0)}\rangle + |\phi^{(1)}\rangle + |\phi^{(2)}\rangle + \dots,$$

$$\lambda(k) = \lambda^{(1)}(k) + \lambda^{(2)}(k) + \dots,$$

where $|\phi^{(n)}\rangle \sim \lambda^{(n)} \sim v^n \sim \varepsilon(k)^n$. Notice that we have not considered the order zero in λ because we are perturbing the critical point. The order zero gives

$$\mathcal{L}_0^c|\phi^{(0)}\rangle = 0 \Rightarrow |\phi^{(0)}\rangle = \beta_1|1\rangle + \beta_0|0\rangle + \beta_{-1}|-1\rangle.$$

The first order gives

$$\mathcal{L}_0^c|\phi^{(1)}\rangle = [\lambda^{(1)}(k) - (\varepsilon(k)\Delta\mathcal{L}_0 - ivk_c\mathcal{L}_1)]|\phi^{(0)}\rangle = |b^{(1)}\rangle.$$

Hence, in the first order, we must impose the solvability conditions

$$\langle 1|b^{(1)}\rangle = 0, \quad \langle 0|b^{(1)}\rangle = 0 \quad \text{and} \quad \langle -1|b^{(1)}\rangle = 0,$$

which lead to the eigenvalues problem

$$\begin{pmatrix} \varepsilon(k) & -\frac{ik_c v}{2} & 0 \\ -\frac{ik_c v}{2} & 0 & -\frac{ik_c v}{2} \\ 0 & -\frac{ik_c v}{2} & \varepsilon(k) \end{pmatrix} \begin{pmatrix} \beta_1 \\ \beta_0 \\ \beta_{-1} \end{pmatrix} = \lambda^{(1)}(k) \begin{pmatrix} \beta_1 \\ \beta_0 \\ \beta_{-1} \end{pmatrix}.$$

Therefore, it is obtained

$$\lambda_1^{(1)}(k) = \varepsilon(k), \quad (11)$$

$$\lambda_{\pm}^{(1)}(k) = \frac{\varepsilon(k)}{2} \pm i\sqrt{\frac{(k_c v)^2}{2} - \left(\frac{\varepsilon(k)}{2}\right)^2}, \quad (12)$$

with the eigenvectors

$$|\phi^{(0)}\rangle_1 = |1\rangle - |-1\rangle,$$

$$|\phi^{(0)}\rangle_{\pm} = |1\rangle - \frac{ik_c v}{\lambda_{\pm}^{(1)}(k)}|0\rangle + |-1\rangle.$$

Therefore, at least for low speed, the instability always involves the conjunction of three modes. In contrast with the case of non-self-propelled particles, here, the mode $m = 0$ is always excited during the finite wavelength instability.

Figure 2 compares the perturbation theory and a numerical computation of the $\lambda(k)$ spectrum for low speed. To wit, we have solved the eigenvalues problem (5) in the truncated basis

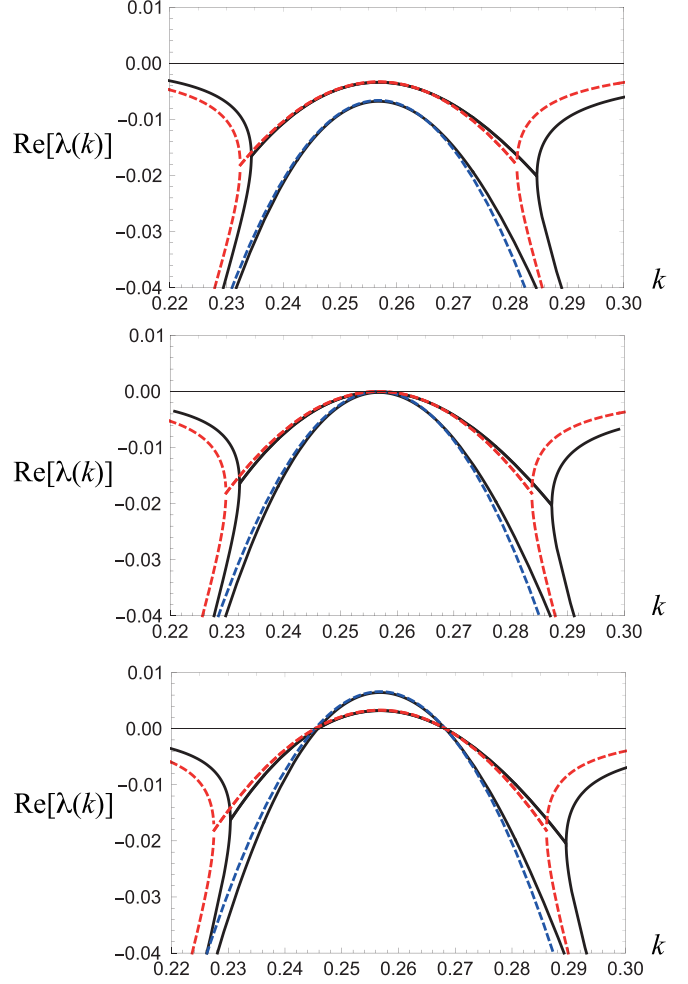


FIG. 2. Computations of the $\lambda(k)$ spectrum near criticality for low speed $v = 0.1$, and: (top) below criticality $n_0 a = n_0 a_c + 0.1$; (middle) critical point $n_0 a = n_0 a_c$; (bottom) above criticality $n_0 a = n_0 a_c - 0.1$, with $n_0 a_c \cong -3.78$. Other parameters as in Fig. 1. Continuous lines correspond to solutions of the eigenvalues problem (5) in the truncated basis $\{e^{im\theta}\}_{m=-10}^{10}$. Dashed lines correspond to the perturbation theory estimations (11) and (12).

$\{e^{im\theta}\}_{m=-10}^{10}$. Both approaches show a good agreement near the instability and close to the critical wave number.

Furthermore, at the critical point, the instability takes place with the oscillatory frequency

$$\omega \approx \frac{k_c v}{\sqrt{2}} + \mathcal{O}(v^3), \quad (13)$$

that is, it corresponds to the type I_o in the Cross-Hohenberg classification of instabilities [14].

3. Finite wavelength instability for arbitrary speed

For arbitrary speed, we have computed the $\lambda(k)$ spectrum by solving the eigenvalues problem (5) in the truncated basis $\{e^{im\theta}\}_{m=-M}^M$. Figure 3 displays the typical form of the spectrum above the instability. It shows the same features as for low speed, the confluence of three modes, two of them with a nonzero imaginary part. That is, it is a type I_o instability.

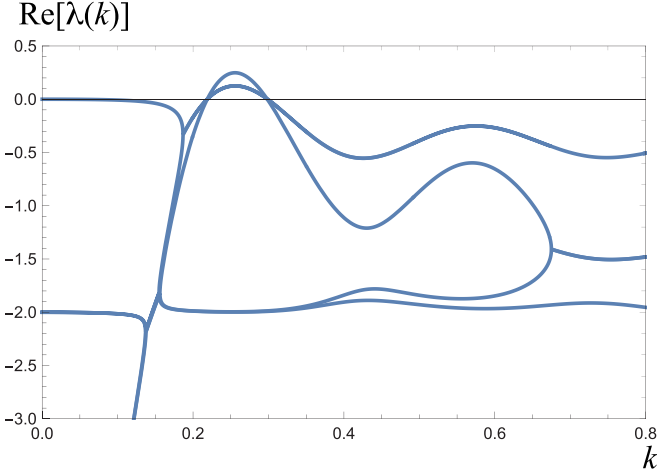


FIG. 3. Numerical computation of the $\lambda(k)$ spectrum in the truncated basis $\{e^{im\theta}\}_{m=-10}^{10}$ with $n_0a = -12$, $v = 2.5$, $\sigma = 20$, and $\eta = 1$.

Far from criticality, as shown in Fig. 4, the intricate splitting structure of the $\lambda(k)$ spectrum branches might occur inside the band of unstable wave numbers. Nevertheless, close to the critical point, the instability shows again the same features (see dashed lines in Fig. 4).

However, the branch that starts from $\lambda(k=0) = 0$ quickly falls down for high speed. The top panel of Fig. 5 displays this phenomenon. It can be attributed to the diffusive effect of the speed, which tends to disorder the particles. In fact, the dashed curve in the top panel of Fig. 5 corresponds to the perturbative estimation (10). Hence, in this high-speed case, the instability involves only two modes. As shown in the middle panel of Fig. 5, at the critical wave number k_c , the unstable eigenvalues have a nonzero imaginary part. Therefore, it is still a type- I_0 instability.

Furthermore, expanding the eigenfunction Φ in the basis $\{e^{im\theta}\}_{m=-\infty}^{\infty}$,

$$\Phi = \sum_{m=-\infty}^{\infty} \beta_m e^{im\theta}, \quad (14)$$

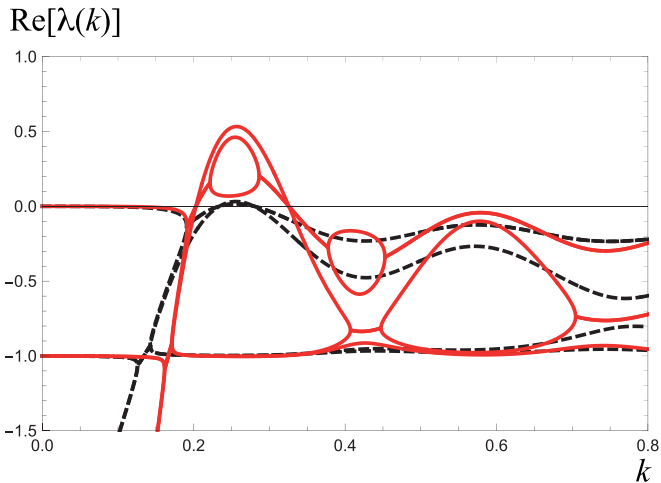


FIG. 4. Numerical computation of the $\lambda(k)$ spectrum in the truncated basis $\{e^{im\theta}\}_{m=-10}^{10}$ with $v = 1$, $\sigma = 20$, and $\eta = 0.5$. Continuous lines correspond to $n_0a = -12$, while dashed lines to $n_0a = -4.5$.

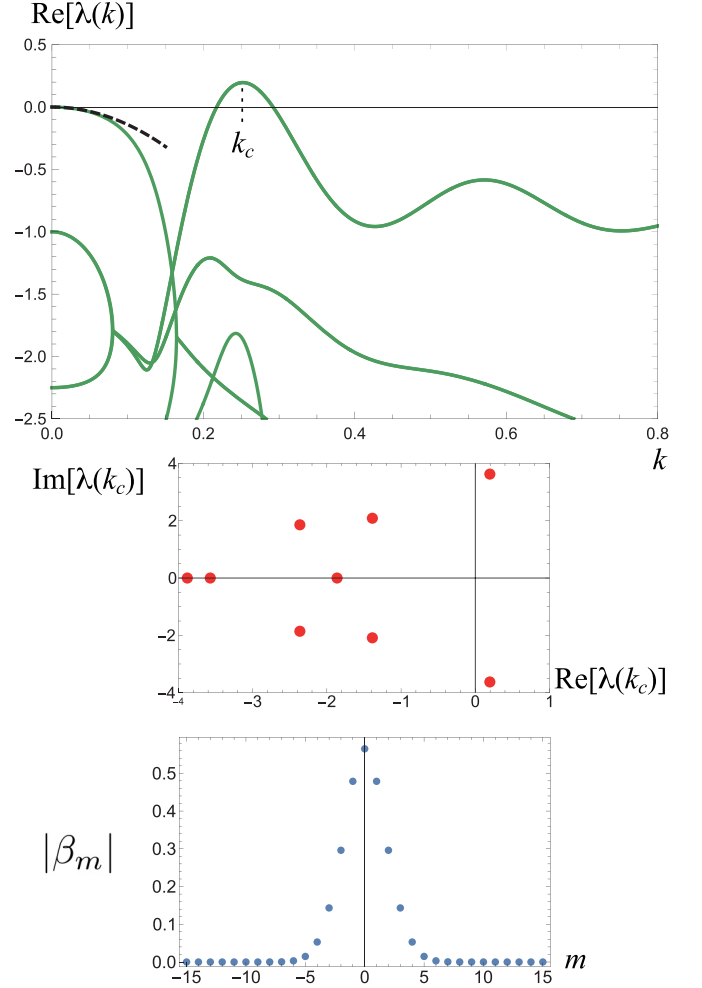


FIG. 5. Numerical computation of the $\lambda(k)$ -spectrum in the truncated basis $\{e^{im\theta}\}_{m=-15}^{15}$ for high speed $v = 17$. Other parameters are $n_0a = -20$, $\sigma = 20$, and $\eta = 0.5$. (Top) $\lambda(k)$ spectrum, the dashed curve corresponds to the perturbative estimation (10). $k_c \cong 0.2521$. (Middle) Eigenvalues at k_c . (Bottom) $|\beta_m|$, as defined in Eq. (14), for the unstable eigenvalues shown in the middle panel.

one may estimate the coefficients β_m by using the truncation approach. Notice that the β coefficients associated with both unstable eigenvalues have the same module. The bottom panel of Fig. 5 shows our results for the most unstable wave number k_c (also showing that the truncation with $M = 15$ is pretty conservative). That is, we are displaying $|\beta_m|$ for the unstable eigenvalues shown in the middle panel. Here, again, the mode $m = 0$ is strongly excited during the instability.

III. NUMERICAL OBSERVATIONS ABOVE THE INSTABILITY

In this section, we present some numerical observations above the instability. To wit, we have simulated the equations of motion (1) and (2), using an Euler-Maruyama method, in a square box of size $L = 100$ with periodic boundary conditions and null-flux boundary conditions. For the null-flux, we have considered a perfect reflection of the particles in the walls.

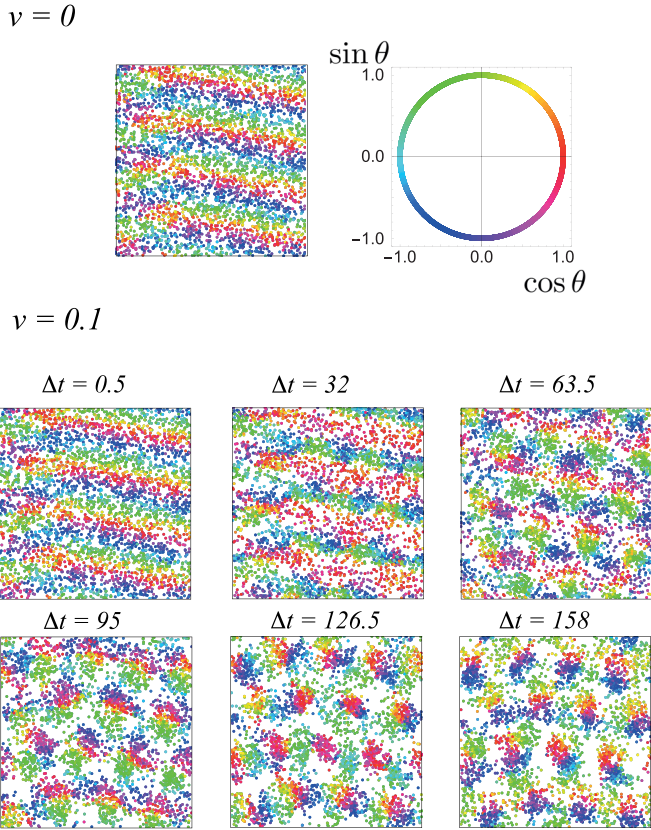


FIG. 6. (Top) Non-self-propelled particles $v = 0$, other parameters are $n_0 a = -12$, $\sigma = 20$, $\eta = 0.5$, $N = 4000$, and $dt = 0.05$. The system is initialized with randomly distributed positions and polarizations. The top-left panel shows the particle's position in the box, and the top-right panel shows the θ -angle distribution in a unitary circle after a time $t \sim 10^4$ has elapsed from the initial condition. (Bottom) Same as top panels, but with $v = 0.1$. The initial condition is the state shown in the top panels, and Δt is the time elapsed from this initial condition.

A. Periodic boundary conditions

Let us start exploring the case $v = 0$. Here, there is no movement of the particles; therefore, the initial spatial distribution of particles is preserved during the system evolution. It is like a disordered lattice. The top panel of the Fig. 6 shows the steady state of this non-self-propelled system for parameters above the finite wavelength instability. The system has been initialized with randomly distributed positions and orientations; after a transient, the particle polarizations form a stripe pattern. This configuration seems static (except by small fluctuations) for long-time simulations ($t \sim 10^4$). Notice that the pattern wave number $k = 8\pi/L \cong 0.251$ is inside the band of unstable wave numbers $k \in [0.202, 0.328]$.

The bottom panels of Fig. 6 display the effect of adding a low speed to the particles in the static stripe pattern. Due to the movement, the particles begin forming clusters with mostly the same polarization. These clusters self-organize in hexagonal configurations. The new pattern becomes clearer after a long transient ($t \sim 10^4$). Figure 7 shows it. The system forms a neat hexagonal structure, where the active particles

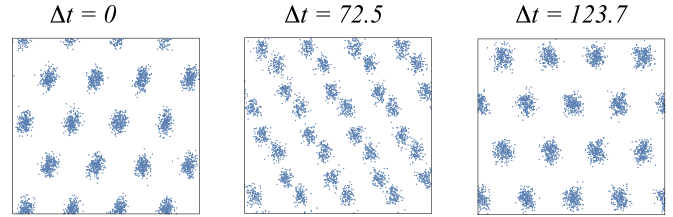


FIG. 7. Same as bottom panels of Fig. 6, but after a long transient $t_0 \sim 10^4$. $\Delta t = t - t_0$.

perform some kind of dance alternating between a hexagonal configuration of clusters and a striped lineup of clusters.

For $v = 1$ the formed pattern is quite similar, as shown in Fig. 8, where we reinitialized the system with randomly distributed positions and orientations. Here, again, the system forms a hexagonal structure, where the active particles are switching between a hexagonal configuration of clusters, a hexagonal configuration of empty sites, and a striped lineup of clusters. The stripe patterns always take place in one of the three crystal lines of the hexagonal net, which seems to have a quite stable orientation. The underlying dynamics of this kind of standing wave consists of the superposition of two counterpropagating and purely hexagonal traveling waves. They are assembling and disassembling a global hexagonal structure and a striped lineup of particles. MOV1 in the Supplemental Material [33] shows it. During the self-assembling process, the propagation direction of the counterpropagating hexagonal waves changes. These changes seem quite erratic, as discussed in the next section. Moreover, the hexagonal configuration of empty sites is an intermediate step between

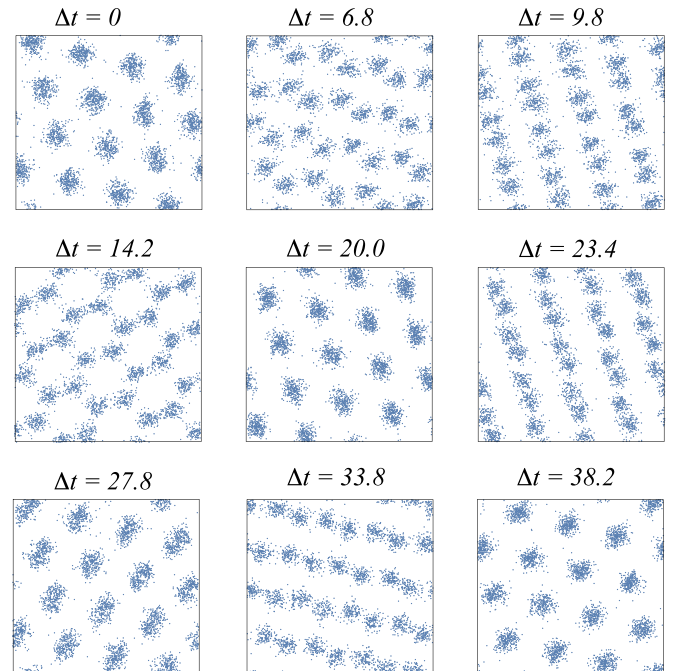


FIG. 8. Same as Figs. 6 and 7, except that $v = 1$. The system has been initialized with randomly distributed positions and orientations; after a transient $t_0 \sim 10^3$, particle positions are shown at different $\Delta t = t - t_0$.

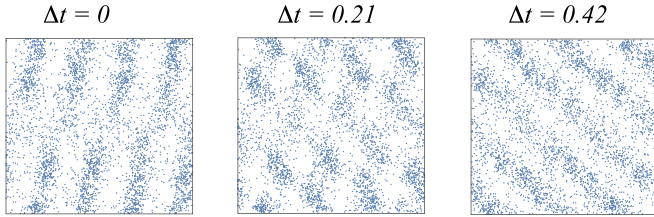


FIG. 9. Simulation with $v = 17$, $n_0 a = -20$, $\sigma = 20$, $\eta = 0.5$, and $dt = 0.01$. The system has been initialized with randomly distributed positions and orientations; after a transient $t_0 \sim 10^2$, particle positions are shown at different $\Delta t = t - t_0$.

the global hexagonal net and the particle's lineup, which only sometimes appears because the reassembling might occur in the same crystalline line where the lineup takes place. As we discuss in the next section, here, again, the selected wave number is inside the band of unstable wave numbers.

Furthermore, we have observed similar dancing in many of our numerical explorations in the parameters space. However, the two counterpropagating hexagonal waves do not seem to dance in other cases. For example, the formed pattern has a more regular behavior in time for high speed. Figure 9 displays it. The system is switching between stripe patterns with different orientations. The underlying dynamics is, again, related to two counterpropagating hexagonal waves (with a higher dispersion of particles in this case). Here, however, they do not seem to change their propagation direction. Since the dancing hexagons are the most intricate nonequilibrium structure formed after the instability, we will focus on them for the rest of the paper.

B. Null-flux boundary conditions

Null-flux boundary conditions may preclude the counterpropagation of the hexagonal waves. It is worth noticing, however, that the finite wavelength instability does not depend on the boundary conditions. They may affect, at most, the wave-number selection. Figure 10 displays a simulation for the same parameters and initial condition as Fig. 8 but with null-flux boundary conditions. The formed pattern is pretty defective. In the movie (MOV2 in the Supplemental Material [33]), it is possible to appreciate its dynamics. There are still two counterpropagating hexagonal waves colliding with the walls, precluding the system from reaching the same level of synchrony as in the case of periodic boundary conditions. Nevertheless, the phenomenon is still there.

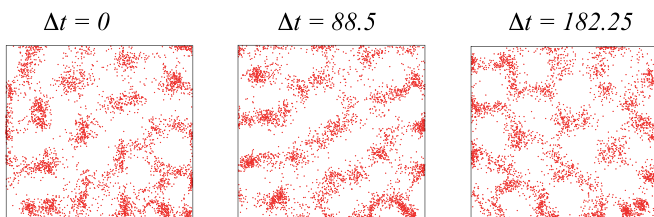


FIG. 10. Same as Fig. 8, but with null-flux boundary conditions.

IV. SPATIOTEMPORAL PATTERN DYNAMICS

In this section, we propose an approach to characterize the dynamics of dancing hexagons.

A. Spatial structuring

Let us consider the coarse-grained density of particles,

$$\mathcal{N}_\Delta(\vec{r}, t) = \int_{x-\Delta/2}^{x+\Delta/2} \int_{y-\Delta/2}^{y+\Delta/2} \frac{dx' dy'}{\Delta^2} \int_0^{2\pi} n(\vec{r}', \theta, t) d\theta, \quad (15)$$

with the density $n(\vec{r}, \theta, t)$ defined as in Eq. (3), and $\vec{r} = (x, y)$.

It is worth noticing that, neglecting the fluctuations inside the grains, we may approach

$$\mathcal{N}_\Delta(\vec{r}, t) \approx N \int_0^{2\pi} \rho(\vec{r}, \theta, t) d\theta,$$

expanding

$$\rho(\vec{r}, \theta, t) = \sum_{m=-\infty}^{\infty} P_m(\vec{r}, t) e^{im\theta},$$

it is obtained

$$\mathcal{N}_\Delta(\vec{r}, t) \approx 2\pi N P_0(\vec{r}, t).$$

Therefore, the excitation of the mode $m = 0$ seems to be crucial for observing spatial structuring. Otherwise, we may only observe polarization patterns, as in the case of zero speed $v = 0$ (as, for example, in the top panel of Fig. 6).

Then, we introduce the normalized Fourier transform of (15),

$$\mathcal{F}_\Delta(\vec{k}, t) = \frac{1}{N} \int_0^L \int_0^L \mathcal{N}_\Delta(\vec{r}, t) e^{i\vec{k}\cdot\vec{r}} dx dy, \quad (16)$$

and

$$f_\Delta(\vec{k}, t) = |\mathcal{F}_\Delta(\vec{k}, t)|. \quad (17)$$

Figure 11 shows $f_\Delta(\vec{k}, t)$, and compares with the spatial particles distribution.

For the parameters shown in Fig. 11 [where we used the same numerical data as in Fig. 8 and MOV1 in the Supplemental Material [33], the system selects, let us say, the wave vector

$$\vec{k}_1 = (6\pi/L, -6\pi/L),$$

together with the resonant ones, \vec{k}_2 (a rotation on $2\pi/3$ of \vec{k}_1) and \vec{k}_3 (a rotation on $4\pi/3$ of \vec{k}_1). That is, a resonant triad $\vec{k}_1 + \vec{k}_2 + \vec{k}_3 = 0$. These three modes are equally excited when assembling the global hexagonal structure. The hexagonal structure of peaks exhibited by $f_\Delta(\vec{k}, t)$, and shown in the top panel of Fig. 11, corresponds to the tips of the six vectors $\pm\vec{k}_j$, with $j = 1, 2, 3$. In contrast, during the lineups, one mode dominates over the other two. For instance, in the bottom panel of Fig. 11, the dominant mode is \vec{k}_3 . Moreover,

$$k = |\vec{k}_1| = |\vec{k}_2| = |\vec{k}_3| \cong 0.267$$

is inside the band of unstable wave numbers $k \in [0.203, 0.326]$.

The right panels of Fig. 11 compare the spatial particle distribution and a reconstructed density from the dominant

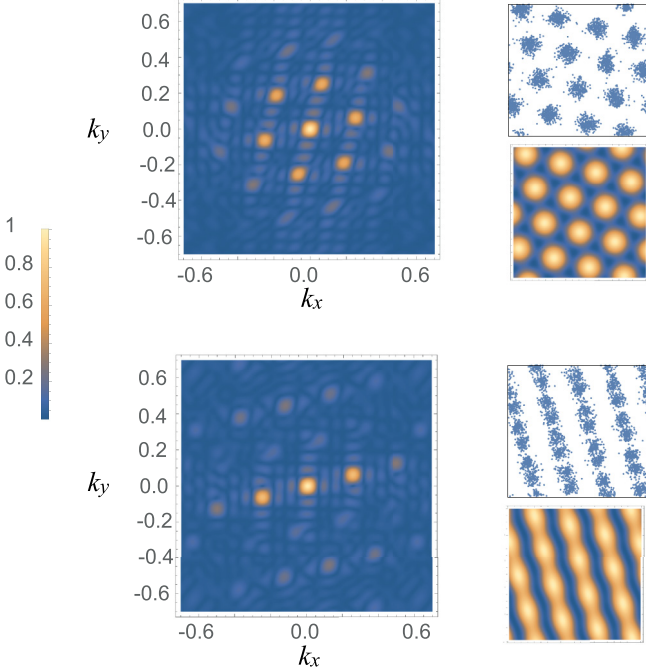


FIG. 11. (Left) Density plots of $f_{\Delta}(\vec{k}, t)$, as defined in Eq. (17), for $\Delta = 5$. (Right) The states that are related to the Fourier transforms showing in the left panels. We have used the same numerical data that we used in Fig. 8 and movie (MOV1 in the Supplemental Material [33]).

Fourier modes, that is, once the high harmonic components are filtered. It gives a good picture of the patterns that the system forms in a given time. Figure 12 displays the time evolution of the module of the amplitudes related to the vectors of the resonant triad. These amplitudes oscillate, switching between one predominant amplitude (stripes) to three equally likely amplitudes (hexagons). The amplitudes oscillation becomes quite erratic for longer time simulations, seeming to be aperiodic.

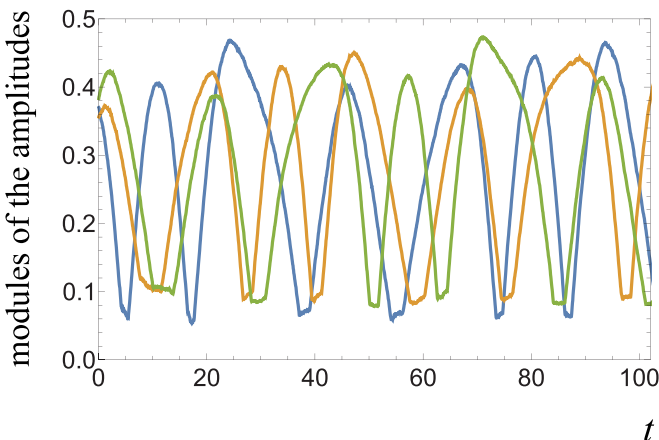


FIG. 12. Amplitudes extracted from the Fourier transform of the coarse-grained spatial density (peaks of $f_{\Delta}(\vec{k}, t)$, as defined in Eq. (17), with $\Delta = 5$) for the same numerical data used in Fig. 8 and movie (MOV1 in the Supplemental Material [33]).

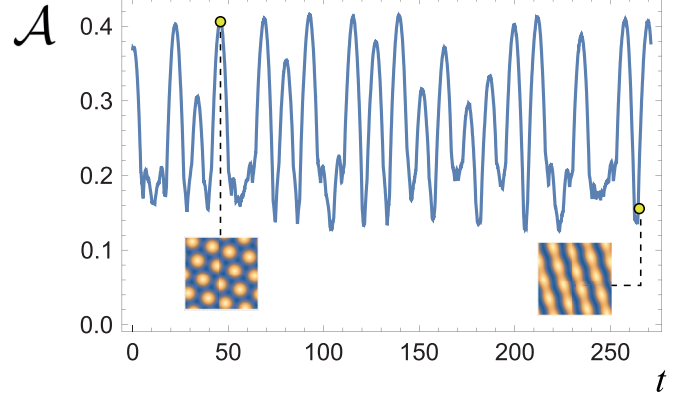


FIG. 13. Geometrical average of the amplitudes, as defined in Eq. (18), for the same numerical data used in Fig. 12 (notice that we are showing a larger time window).

Denoting by A_j the amplitude related to the wave vector \vec{k}_j , with $j \in \{1, 2, 3\}$, one may compute the geometrical average

$$\mathcal{A} = \sqrt[3]{|A_1 A_2 A_3|}. \quad (18)$$

Figure 13 shows it. As larger as \mathcal{A} is, the three amplitudes are more similar (hexagons), while the smaller \mathcal{A} are related to a dominant amplitude (stripes).

B. Polarization dynamics

Now, we will consider the normalized coarse-grained density of orientational angles,

$$\vartheta_{\delta}(\theta, t) = \frac{1}{N} \int_{\theta-\delta/2}^{\theta+\delta/2} d\theta' \int_0^L \int_0^L dx' dy' n(\vec{r}', \theta', t), \quad (19)$$

which may be described by the vector

$$\vec{\vartheta}_{\delta}(\theta, t) = \vartheta_{\delta}(\theta, t) \hat{\theta} = (\vartheta_x, \vartheta_y), \quad (20)$$

where $\hat{\theta} = (\cos \theta, \sin \theta)$. Figure 14 displays lobules that represent these coarse-grained polarization distributions. More precisely, a lobule corresponds to the curve described by $\vec{\vartheta}_{\delta}(\theta)$ as we move θ .

The lobules rotate in time, also changing their elongation. To characterize this movement, we have used the inertia tensor

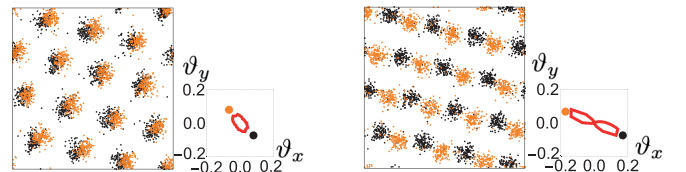


FIG. 14. The two counterpropagating hexagons forming (left) the global hexagonal network and (right) a striped lineup. Beside each configuration, it is shown $\vec{\vartheta}_{\delta}(\theta, t) = (\vartheta_x, \vartheta_y)$, as defined in Eq. (20), with $\delta = \pi/12$. We have used the same numerical data that we used in Fig. 8 and movie (MOV1 in the Supplemental Material [33]).

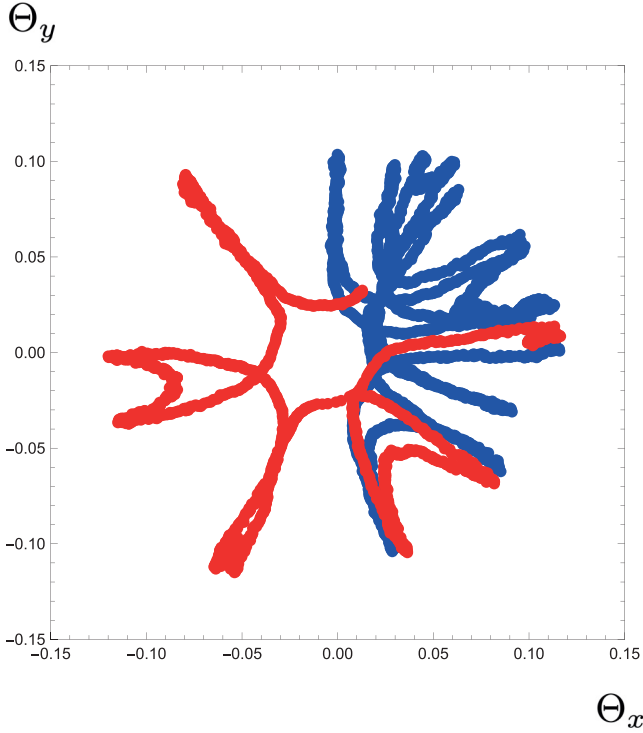


FIG. 15. $\vec{\Theta}(t) = (\Theta_x, \Theta_y)$, as defined in Eq. (21), with $\delta = \pi/12$. The different tonalities of the time series correspond to time windows of: the first $\Delta T = 87.6$ (periodic movement); and after $\Delta T = 100$ (erratic burst). Since the sign of \hat{e}_- can be arbitrarily settled, we have chosen the one that gives continuity to the time series. We have used the same numerical data that we used in Fig. 8 and movie (MOV1 in the Supplemental Material [33]).

formalism; that is, we have defined the inertiallike matrix

$$\mathcal{I} = \sum_{\theta \in \Omega} \begin{pmatrix} \vartheta_x^2 & -\vartheta_x \vartheta_y \\ -\vartheta_x \vartheta_y & \vartheta_y^2 \end{pmatrix},$$

where Ω represents all the points of the discretization ($2\pi/\delta$ in this case). Then, we solve the eigenvalues problem

$$\mathcal{I} \hat{e}_{\pm} = \Lambda_{\pm} \hat{e}_{\pm},$$

where Λ_+ is the largest eigenvalue, while Λ_- is the lowest one (noting that \mathcal{I} is positive defined). The unitary vectors \hat{e}_{\pm} are, then, the principal axis of the lobule. The direction of maximum elongation is related to the lowest inertial-like momentum, that is, with the axis \hat{e}_- . On the other hand, the elongation may be quantified by the largest inertial-like momentum Λ_+ (the resistance to a hypothetical rotation around \hat{e}_+). Therefore, we define the order parameter

$$\vec{\Theta}(t) = \Lambda_+ \hat{e}_- = (\Theta_x, \Theta_y). \quad (21)$$

Figure 15 displays the time evolution of $\vec{\Theta}(t)$, showing a pretty intricate movement. Initially, it seems a periodic movement (complicated but periodic); however, as time runs (note the change in the tonality), the lobule dynamics undergoes a turbulent burst, where its movement becomes quite erratic. The last event is a signature of intermittence.

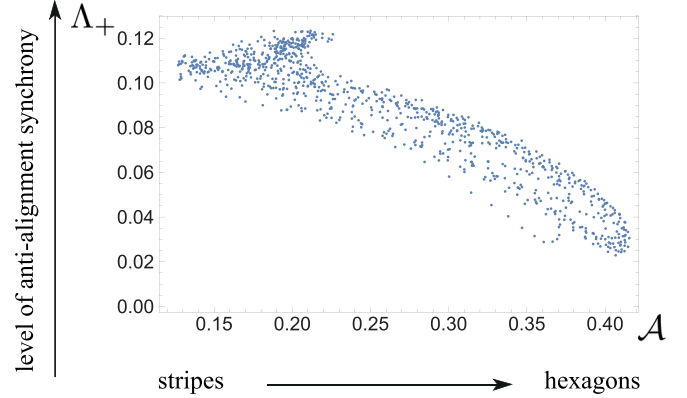


FIG. 16. Λ_+ versus \mathcal{A} [as defined in Eq. (18)], for the same numerical data used in Fig. 8 and MOV1 in the Supplemental Material [33].

Moreover, the lobules' shape suggests that the level of anti-alignment synchrony (how many particles are in anti-alignment) is lower when the system forms the global hexagonal configuration. In fact, as shown in Fig. 14, the lobule looks more elongated when the particles are forming the striped lineup. Note that Λ_+ is a measurement of such kind of out-of-equilibrium antiferromagnetic ordering (how elongated is a lobule). Figure 16 shows Λ_+ versus the geometric average of the amplitudes \mathcal{A} [as defined in Eq. (18)]. Therefore, the level of anti-alignment synchrony is lower in the global hexagonal configuration, probably because the changes in the counterpropagation direction (along the different crystalline lines) occur when the system forms such configurations (see the rotation of $\vec{\Theta}$ in Fig. 15).

V. BRIEF NUMERICAL EXPLORATION IN THE VICSEK'S MODEL

Although none of the analytical findings we have found for the Kuramoto-like dynamics are directly accessible for Vicsek's model, we may test if anti-aligning interaction induces similar behaviors. To do it, we consider the original version of this model, that is, with the same discretization, updates, and noise [15]. But, we modified the interaction term to incorporate anti-aligning interaction. More precisely, we consider the discrete evolution of the orientation angles and positions,

$$\theta_l(t+1) = F_l + \Delta\theta_l \quad (22)$$

$$\vec{r}_l(t+1) = \vec{r}_l(t) + v\hat{\theta}_l(t+1), \quad (23)$$

where $\Delta\theta_l$ is a random variable uniformly distributed in $[-\eta/2, \eta/2]$. For the interaction term, we have considered

$$F_l = \langle \theta(t) \rangle_{\mathcal{D}_\sigma[\vec{r}_l(t)]} + \pi,$$

where the first term corresponds to the average angle, in the circular domain $\mathcal{D}_\sigma[\vec{r}_l(t)]$, computed accordingly with the Vicsek's prescription [15]. Therefore, we have only summed π to Vicsek's original interaction term. That is, the particle tends to anti-align with its around.

As shown in Fig. 17, we have found dancing hexagons in this model. The movie (MOV3 in the Supplemental Material

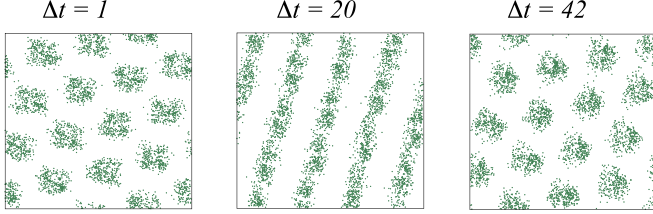


FIG. 17. Numerical simulation of the equations of motion (22) and (23), for $v = 0.05$, $\eta = 0.2$, $\sigma = 2$, and $N = 4000$, in a square box of size $L = 10$ with periodic boundary conditions. The system is initialized with randomly distributed positions and orientations; after a transient $t_0 \sim 10^5$, particle positions are shown at different $\Delta t = t - t_0$.

[33]) displays its dynamics, which looks quite similar to the one exhibited by the Kuramoto-like model (see MOV1 in the Supplemental Material [33]). Furthermore, the system selects the same wavelength, perhaps, because we used the same ratio σ/L .

Figure 18 shows $\vec{\Theta}$, as defined in Eq. (21), computed for the dancing hexagons of the Vicsek's model. The $\vec{\Theta}$ trajectory looks more dispersed than in the case of the Kuramoto-like model, perhaps because of the discrete-time dynamics. Notice that we have emphasized a single rotation of the $\vec{\Theta}$ vector. As in the Kuramoto-like model, the $\vec{\Theta}$ vector does not always

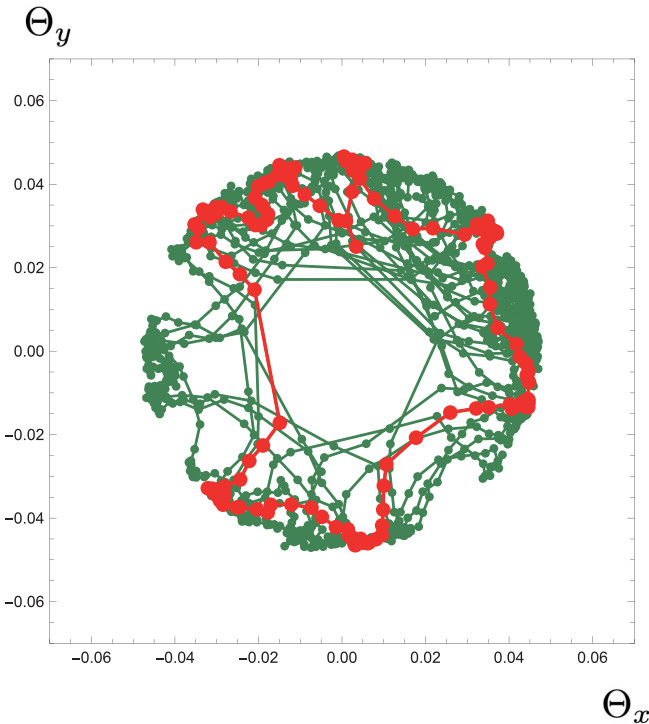


FIG. 18. $\vec{\Theta}(t) = (\Theta_x, \Theta_y)$, as defined in Eq. (21), with $\delta = \pi/12$, for the Vicsek's model (22) and (23). We have used the same numerical data that we used in Fig. 17 and movie (MOV3 in the Supplemental Material [33]). Since the sing of \hat{e}_- can be arbitrarily settled, we have chosen the one that gives continuity to the time series.

show a neat rotation, instead remaining in the same direction of counterpropagation for a long time (the denser zones in the Fig. 18). Furthermore, for other parameters, the two hexagonal waves merely counterpropagate without dancing, periodically assembling and disassembling a stripe pattern.

VI. CONCLUSIONS AND FUTURE PROSPECTS

In summary, we have found that anti-aligning interaction induces a finite wavelength instability. The instability takes place with a nonzero imaginary part of the critical modes of the $\lambda(k)$ spectrum (it is a type- I_o instability in the Cross-Hohenberg nomenclature [14]). Consequently, the system exhibits pattern formation. The formed pattern can be described as the dance of two counterpropagating hexagons. They are assembling and disassembling a global hexagonal structure and a striped lineup of particles. These dance steps become quite erratic for long-time simulations, showing turbulent bursts and seeming aperiodic. We have observed similar dancings in many of our numerical explorations in the parameters space; however, the global hexagonal structure's reassembling might sometimes be shifted. In contrast, striped lineups are always pretty neat. Furthermore, for other parameters, the two hexagonal traveling waves merely counterpropagate without dancing (as in the high-speed case documented here), periodically forming the stripe pattern across the crystalline line of the hexagonal net.

Of course, a more extensive numerical study of pattern formation must be addressed in future works. Preliminarily, we have not observed hysteresis in the formed patterns. Moreover, the dancing hexagons' dynamics suggests the presence of spatiotemporal chaos. In particular, burst events are usually related to intermittence. From direct numerical simulations of the equations of motion (1) and (2), it is hard to distinguish chaos from noise. A weakly nonlinear analysis may help to elucidate both the transition to self-organization and the presence of chaotic attractors.

To end, we performed a brief numerical exploration in Vicsek's model, finding dancing hexagons for anti-aligning interaction. The occurrence of a finite wavelength instability here still has to be elucidated, perhaps using the Bonilla and Trenado approach [28], based on Ihle's kinetic theory [17]. In fact, they have put forward the general linear stability problem when anti-alignments appear as fluctuations. It might be easy to generalize for the model equations (22) and (23). However, as Bonilla and Trenado pointed out, it seems complicated to solve for finite wavelengths; in fact, they presented a perturbative solution for small wave numbers, finding a zero wave-number Hopf instability [28]. This type of instability should be absent in the fully anti-aligning systems considered here (as shown in Sec. II B 1 for the Kuramoto-like model). At any rate, it seems a promising line to explore in future works.

ACKNOWLEDGMENT

I would like to thank FONDECYT, Project No. 1211251, for financial support.

- [1] Y. Kuramoto, in *International Symposium on Mathematical Problems in Theoretical Physics*, edited by H. Arakai, Lecture Notes in Physics Vol. 39 (Springer, New York, 1975), p. 420.
- [2] Y. Kuramoto, *Chemical Oscillations, Waves and Turbulence* (Springer-Verlag, Berlin, 1984).
- [3] S. H. Strogatz, *Physica D* **143**, 1 (2000).
- [4] A. Pikovsky, M. Rosenblum, and J. Kurths, *Synchronization: A Universal Concept in Nonlinear Sciences* (Cambridge University Press, Cambridge, 2001).
- [5] S. C. Manrubia, A. S. Mikhailov, and D. H. Zanette, *Emergence of Dynamical Order: Synchronization Phenomena in Complex Systems* (World Scientific, Singapore, 2004).
- [6] J. A. Acebrón, L. L. Bonilla, C. J. Pérez-Vicente, F. Ritort, and R. Spigler, *Rev. Mod. Phys.* **77**, 137 (2005).
- [7] Y. B. Zeldovich, *Selected Works of Yakov Borisovich Zeldovich*, Vol. I: Chemical Physics and Hydrodynamics (Princeton University Press, Princeton, 1992).
- [8] A. M. Turing, *Phil. Trans. R. Soc. B* **237**, 37 (1952).
- [9] R. Lefever, *Phil. Trans. R. Soc. A* **376**, 20170365 (2018).
- [10] S. Chandrasekhar, *Hydrodynamic and Hydromagnetic Stability* (Oxford University Press, Oxford, 1961).
- [11] L. A. Lugiato and R. Lefever, *Phys. Rev. Lett.* **58**, 2209 (1987).
- [12] R. Lefever and O. Lejeune, *Bull. Math. Biol.* **59**, 263 (1997); C. A. Klausmeier, *Science* **284**, 1826 (1999); J. A. Sherratt, *Proc. Natl. Acad. Sci. USA* **112**, 4202 (2015).
- [13] M. A. Fuentes, M. N. Kuperman, and V. M. Kenkre, *Phys. Rev. Lett.* **91**, 158104 (2003); E. Hernandez-Garcia and C. Lopez, *Phys. Rev. E* **70**, 016216 (2004); M. G. Clerc, D. Escaff, and V. M. Kenkre, *ibid.* **72**, 056217 (2005); **82**, 036210 (2010); E. Heinsalu, E. Hernandez-Garcia, and C. Lopez, *ibid.* **85**, 041105 (2012).
- [14] M. C. Cross and P. C. Hohenberg, *Rev. Mod. Phys.* **65**, 851 (1993).
- [15] T. Vicsek, A. Czirók, E. Ben-Jacob, I. Cohen, and O. Shochet, *Phys. Rev. Lett.* **75**, 1226 (1995).
- [16] G. Grégoire and H. Chaté, *Phys. Rev. Lett.* **92**, 025702 (2004); M. Nagy, I. Daruka, and T. Vicsek, *Physica A* **373**, 445 (2007); M. Aldana, V. Dossetti, C. Huepe, V. M. Kenkre, and H. Larralde, *Phys. Rev. Lett.* **98**, 095702 (2007); H. Chaté, F. Ginelli, G. Grégoire, and F. Raynaud, *Phys. Rev. E* **77**, 046113 (2008).
- [17] T. Ihle, *Phys. Rev. E* **83**, 030901(R) (2011); Y.-L. Chou, R. Wolfe, and T. Ihle, *ibid.* **86**, 021120 (2012); T. Ihle, *Eur. Phys. J.: Spec. Top.* **224**, 1303 (2015).
- [18] L. L. Bonilla and C. Trenado, *Phys. Rev. E* **98**, 062603 (2018).
- [19] F. D. C. Farrell, M. C. Marchetti, D. Marenduzzo, and J. Tailleur, *Phys. Rev. Lett.* **108**, 248101 (2012).
- [20] D. Escaff and R. Delpiano, *Chaos* **30**, 083137 (2020).
- [21] A. P. Solon, H. Chaté, and J. Tailleur, *Phys. Rev. Lett.* **114**, 068101 (2015).
- [22] F. Peruani, T. Klaus, A. Deutsch, and A. Voss-Boehme, *Phys. Rev. Lett.* **106**, 128101 (2011); F. Ginelli, F. Peruani, M. Bar, and H. Chaté, *ibid.* **104**, 184502 (2010).
- [23] D. Escaff, *Chaos* **33**, 043137 (2023).
- [24] N. Kruk, Y. Maistrenko, and H. Koepl, *Phys. Rev. E* **98**, 032219 (2018).
- [25] B. Liebchen and D. Levis, *Phys. Rev. Lett.* **119**, 058002 (2017); D. Levis, I. Pagonabarraga, and B. Liebchen, *Phys. Rev. Res.* **1**, 023026 (2019).
- [26] F. J. Sevilla, V. Dossetti, and A. Heiblum-Robles, *J. Stat. Mech.* (2014) P12025; V. Dossetti and F. J. Sevilla, *Phys. Rev. Lett.* **115**, 058301 (2015).
- [27] H. Hong and S. H. Strogatz, *Phys. Rev. Lett.* **106**, 054102 (2011).
- [28] L. L. Bonilla and C. Trenado, *Phys. Rev. E* **99**, 012612 (2019).
- [29] K. Wood, C. Van den Broeck, R. Kawai, and K. Lindenberg, *Phys. Rev. Lett.* **96**, 145701 (2006); *Phys. Rev. E* **74**, 031113 (2006).
- [30] K. L. Rodrigues and R. Dickman, *J. Stat. Mech.* (2020) 043406; I. L. D. Pinto, D. Escaff, and A. Rosas, *Phys. Rev. E* **103**, 052215 (2021).
- [31] D. Escaff, I. L. D. Pinto, and K. Lindenberg, *Phys. Rev. E* **90**, 052111 (2014).
- [32] J. W. Cahn and J. E. Hilliard, *J. Chem. Phys.* **28**, 258 (1958); A. J. Bray, *Adv. Phys.* **43**, 357 (1994).
- [33] See Supplemental Material at <http://link.aps.org/supplemental/10.1103/PhysRevE.109.024602> for movies displaying the dynamics that are shown in Figs. 8 (MOV1), 10 (MOV2), and 17 (MOV3).